PCCP

PAPER

View Article Online
View Journal

Cite this: DOI: 10.1039/d6cp00073h

Structural and electronic properties of metal halide perovskites using non-periodic calculations: a combined xTB, DFT, and ONIOM framework

Adrián Moro-Marín, Gregorio García * and Silverio Coco

We present a computational protocol to study the structural and optoelectronic properties of metal halide perovskites using non-periodic calculations (*i.e.*, a cluster-based approach). The proposed framework strategically combines xTB, DFT and ONIOM methods, leveraging their strengths for accurate results with reduced computational cost. Using the $CH_3NH_3PbI_3$ perovskite (MAPI) as a reference system, several cluster models (ranging from 204 to 2175 atoms) were constructed to preserve the chemical environment of the bulk phase and maintain electroneutrality. Structures were optimized with the GFN2-xTB method, while optoelectronic properties were computed at the PBE0-D4/Def2-TZVP level. For the larger systems (>1000 atoms), a two-layer ONIOM scheme was applied, treating the region of interest at the PBE0-D4/Def2-TZVP level, with the rest of the system treated using GFN2-xTB with electrostatic embedding. Our results show that GFN2-xTB is suitable for studying the structural properties of perovskites. Regarding optoelectronic properties, the DFT-calculated bandgap is strongly overestimated for smaller clusters due to nanosizing effects. Meanwhile, for larger systems, results based on a two-layer ONIOM approach significantly enhance the accuracy of computed optoelectronic properties. Overall, this framework offers a reliable and efficient alternative to periodic calculations, broadening the range of computational tools available for studying halide perovskites.

Received 8th January 2026,
Accepted 30th March 2026

DOI: 10.1039/d6cp00073h

rsc.li/pccp

Introduction

In recent years, perovskite solar cells (PSCs) have emerged as a highly promising photovoltaic technology and a competitive alternative to conventional crystalline silicon solar cells. Since their initial development in 2009, PSCs have achieved a remarkable improvement in power conversion efficiency (PCE),[1–18] rising from values below 4% to 27.3% in single-junction devices,[19,20] and up to 35% in perovskites-silicon tandem configurations.[20,21] These high efficiencies were initially achieved using the hybrid organic–inorganic methylammonium lead iodide perovskite ($CH_3NH_3PbI_3$, commonly referred to as MAPI), as well as related materials, such as formamidinium lead iodide (FAPI) perovskite. Their superior features as materials for photovoltaics stem from their outstanding properties, *e.g.*, high compatibility with low-cost solution processing, adequate direct bandgap, high absorption coefficients, small exciton binding energy, ambipolar nature of the carriers and long charge carrier diffusion lengths.[1–18,22–29] Nevertheless, these organic–inorganic perovskites also present important drawbacks, mainly their limited long-term stability and toxicity.[30–32] Currently, there is considerable interest in studying other metal halide perovskites (MHPs) for their use in photovoltaic devices.[1–18,33–38]

The growing interest in this class of materials has led to numerous theoretical studies, primarily aimed at providing an in-depth understanding of the structural and electronic properties of halide perovskites. Among different approaches, theoretical calculations are commonly performed using Density Functional Theory (DFT) in combination with periodic boundary conditions (PBC), with and without the inclusion of relativistic effects.[23,29,33,34,39–60] The results from these periodic calculations are generally limited to the use of pure GGA (Generalized Gradient Approximation) functionals, such as PBE, for studying structural properties. To accurately describe the electronic band structure, hybrid functionals such as PBE0 and HSE06 are commonly employed. These approaches can provide apparently reasonable bandgaps due to fortuitous error cancellation.[49,61] However, in metal halide perovskites, particularly in Pb-based compounds, relativistic effects associated with the heavy Pb atom, such as spin–orbit coupling (SOC), play a crucial role in the accurate description of the electro structure.[43,52,57,62–65] In this sense, PBE0 and HSE06 hybrid

IU CINQUIMA/Química Inorgánica, Facultad de Ciencias, Universidad de Valladolid, 47011 Valladolid, Spain. E-mail: gregorio.garcia@uva.es

functional combined with SOC typically lead to an underestimation of the bandgap compared with experimental values.[23,51,58,59,66] In this context, many-body perturbation theory within the GW framework including SOC is generally considered as reference method for obtaining electronic-structure properties in close agreement with experimental data.[58,59,62–65,67–71] Unfortunately, GW-SOC calculations remain computationally very demanding, particularly for large systems. More recently, other approaches such as the doubly screened dielectric dependent hybrid (DSH) functional,[72] the AK13/GAM exchange functional,[73] the Tran–Blaha modified Becke–Jhonson potential (TB-mBJ)[74] and the DFT-1/2[75–78] methods have also been proposed to improve the description of bandgaps in metal halide perovskites. In addition, TB-mBJ, AK13/GAM and DFT-1/2 methods can often yield accurate bandgaps and represent appealing alternatives to hybrid functionals and GW methods at a significantly lower computational cost.

PBC calculation provide an idealized description of crystalline materials by translational symmetry of the unit cell. Consequently, periodic models may not always capture local phenomena such as local excitations,[79] surface processes,[80,81] structural or point defects,[82] or chemical reactions.[83] In this sense, several studies have shown that electronic excitations in metal halide perovskites may exhibit a partially localized character due to strong electron–phonon coupling, small polaron formation, or defect-induced trap states, which locally break the ideal translational symmetry of the crystal.[84–90] Thus, the electronic wavefunctions derived from cluster models offer advantages for understanding the local properties: molecular orbital theory allows the chemical concepts developed for molecular bonds to be extended to describe chemical bonding at the surface and in the bulk of the material.[91]

As an alternative, less conventional approach involves theoretical studies based on clusters (0D), which represent the fundamental building blocks of bulk systems (3D).[92–99] Such cluster-based models are particularly well suited for describing low-dimensional halide perovskites, such as quantum dots (0D) as well as nanowires (1D), and nanoplatelets or nanosheets (2D).[100–103] These nanostructured systems exhibit size- and shape-dependent optoelectronic properties that differ significantly from their bulk counterparts.[104,105] In this context, minimal clusters can be conceptually related to quantum dots, where strong nanosizing effects are expected.[102,106] From a computational point of view, small clusters are advantageous in terms of reducing computational cost. However, their often differ significantly from PBC calculations when describing to bulk properties, which limits their applicability for studying MHPs.[92,95,97,103,106,107]

To study perovskite materials *via* non-periodic calculations (*i.e.*, a cluster-based approach) by using DFT methods that provide results in agreement with bulk observations, it is necessary to construct larger cluster models which preserve the chemical environment of the ions in the bulk phase.[90,92,102,103,106–109] Although results obtained for clusters consisting of a few hundred atoms or fewer are computationally efficient and useful for comparative analysis (such as assessing the influence of different cations or the choice of exchange–correlation functional), DFT tends to strongly overestimate the bandgap due to nanosizing effects.

In this work, we propose a framework based on non-periodic calculations to study the structural and optoelectronic properties of MHPs, which has allowed us to obtain results consistent with those of the bulk phase. As a starting point, this work focuses on the widely studied MAPI perovskite. Even though, the proposed framework is also applicable to other metal halide perovskites. To ensure computational efficiency without sacrificing accuracy in the obtained results, the proposed framework strategically combines extended Tight-Binding (xTB), DFT and ONIOM methods. To achieve this:

– Firstly, several cluster models were constructed based on the perovskite unit cell, with the aim of preserving the chemical environment of constituent ions (Section 3.1).

– These clusters were optimized using xTB methods,[110] specifically GFN2-xTB (Section 3.2).[111] Although xTB methods were initially developed for the calculation of molecular complexes, J. M. Vicent-Luna *et al.* have shown that xTB methods (specifically a refined version of GFN1-xTB adapted for MHPs) with PBC can achieve accuracy comparable to DFT.[112,113] As seen below, our results demonstrate that GFN2-xTB is sufficiently accurate to describe the structure of MAPI without requiring any additional refinement, while it also enables faster optimizations.

– Finally, electronic band structure and optical absorption were calculated with DFT and time-dependent DFT (TD-DFT), respectively (Section 3.3). The hybrid functional PBE0[114] was used, along with D4 dispersion corrections,[115] in combination with the Def2-TZVP basis set:[116,117] PBE0-D4/Def2-TZVP. Def2 basis sets include an effective core potential (ECP) for heavy elements. The ECPs employed here for Pb are derived from relativistic atomic calculations based on a Dirac–Hartree Fock framework and therefore incorporate scalar relativist effect in an effective manner. While spin–orbit coupling is not treated explicitly in the electronic structure calculation, its main effects are implicitly accounted through the parametrization of the ECP.[118,119]

– For larger systems (>1000 atoms), a two-layer ONIOM[120] scheme with an electrostatic embedding (EE)[121,122] was applied to compute electronic structure-related properties. This method enables an effective partitioning of the system into different regions, each treated at a different level of theory, commonly referred to as the ''high'' and ''low'' levels. Thus, ONIOM allows for the efficient treatment of large systems by studying the region of interest (at the high-level) within a more realistic environment (treated at the low-level). In this sense, the high-level calculation is performed in the presence of the charges of the lower-level region, allowing for proper polarization of the region of interest. In our case, the central region of the cluster was treated at the PBE0-D4/Def2-TZVP theoretical level, while the remaining part of the system was treated using GFN2-xTB. Note that xTB methods are a good choice for the outer region within the ONIOM scheme due to their broad parameterization, reasonable accuracy, and high computational efficiency.[110,111,123–126]

The ONIOM method has been applied to study the electronic structure-related properties of crystals using a cluster-based approach.[120,127–138] In the case of ionic (such as perovskites) or highly polar crystals, where long-range interactions are of great importance due to the slow convergence of the electrostatic potential, the use of EE becomes essential.[134,136–138] Studies combining ONIOM + EE for ionic systems often rely on complex three-layer models,[136–138] which are based on a self-consistent electrostatic embedding scheme, where the cluster model system is embedded in an array of point charges fitted to reproduce the electrostatic crystalline environment. Such approaches require complex setups or usen-driven procedures to generate and integrate the electrostatic potential of the extended lattice. In contrast, our ONIOM + EE approach is based on a two-layer scheme, where ONIOM calculations are performed using standard implementations available in widely used quantum chemistry packages such as ORCA.[139,140] This setup only requires selecting the atoms in the high-level (Section 3.1), significantly streamlining the process.

Computational details

Ground state geometries of built cluster models were optimized using the GFN2-xTB tight-binding method.[110,111] Although the GFN2-xTB method was initially developed to accurately describe molecular structure and non-covalent interactions for large systems with a reduced computational cost,[111,124,141–147] previous studies have shown that a refined version of GFN1-xTB for metal halide perovskites yields results comparable to DFT.[112,113] In our case, GFN2-xTB has proved to be accurate in describing the structure of MAPI without additional refinement. Calculations with GFN2-xTB method were done by using the open-source software xTB.[110]

Based on the optimized structures, single point calculations were done by using PBE0 hybrid functional,[114] along with D4 dispersion corrections,[115] in combination with the Def2-TZVP basis set:[116,117] PBE0-D4/Def2-TZVP theoretical level. The choice of the PBE0 functional[23,59,148,149] and dispersion corrections[46,49,58,150] is based on previous works highlighting their performance in the study MHPs. Meanwhile, the selected basis set includes an Effective Core Potential (ECP) for heavy elements (Pb, and I). In the case of Pb, the use of relativistic ECPs allows for the inclusion of scalar relativist effects in an effective mater, while main effects derived from SOC are accounted for through the parametrization of the ECP.[118,119]

To study optical absorption, vertical transition energies (ΔE_{TD}) for the first fifty excited states were calculated from previously optimized geometries using TD-DFT. Both DFT and TD-DFT calculations were carried out with the ORCA package.[139,140] In ORCA, TD-DFT calculations are performer by default using the Tamm–Dancoff approximation (TDA). TDA approach tends to underestimate strength factors (f); however, it provides accurate results for the energies of the absorption peaks compared to experimental data, while reducing computational cost.[151]

For large clusters with more than 1000 atoms, a two-layer ONIOM[120] scheme was applied to study electronic structure and optical absorption. The central region of the cluster was treated at the PBE0-D4/Def2-TZVP theoretical level, while the remaining part of the system was treated using GFN2-xTB, *i.e.*, PBE0-D4/Def2-TZVP:GFN2-xTB. ONIOM calculations were also carried out with ORCA, which includes electrostatic embedding by default.[121,122]

Molecular plots were generated using the Visual Molecular Dynamics (VMD)[152,153] and MultiWFN[154] software. Multiwfn was also employed to plot Density of States (DOS) and electronic absorption spectra from DFT and TD-DFT calculations, respectively. Thus, discrete energy levels and vertical transitions energies obtained from DFT and TD-DFT calculations were artificially broadened into curves. A normalized Gaussian function, characterized by its full width at half maximum (FWHM), was employed as the broadening function.

Results and discussion

Building the cluster models

Several cluster models were constructed following criteria reported in previous studies on metal-halide perovskites using non-periodic calculations: preserving the chemical environment of the ions in the bulk phase and maintaining electroneutrality.[92,106,107] As shown in Fig. 1(a), the perovskite crystal structure can be described as PbI_6 octahedra located at the corners of a cube, where each octahedron shares a vertex (an iodine atom) with its neighbors. The central cavity the of cube is occupied by a methylammonium (MA) cation. To preserve the chemical environment, each PbI_6 octahedron must also be surrounded by the corresponding methylammonium cations. Therefore, the smallest model defined, referred to as **1-1-1**, consists of eight PbI_6 octahedra and 27 methylammonium cations (Fig. 1b-d). In addition, an electroneutrality criterion was applied, *i.e.*, working with electrically neutral structures by adjusting the number of MA cations, resulting in a stoichiometry of $(CH_3NH_3)_{20}Pb_8I_{36}$ for the cluster **1-1-1**. The removal of these MA cations will lead to distortions in the structure of close PbI_6 octahedra. Therefore, MA cations were removed from the edges of the cluster (*i.e.*, vertices and edge centers), aimed at keeping MA vacancies as far apart as possible. In the case of **1-1-1** cluster, the seven MA vacancies are located at the vertices of the cluster.

Similarly, larger models were also constructed: **2-1-1**, **3-3-3**, **4-3-3** and **4-4-4** (see Fig. 1b-e). The label assigned to each cluster consists of three numbers corresponding to the number of cubes along the *x*–*y*, *x*–*z* and *y*–*z* axes, respectively.

All cluster models were constructed based on the experimental crystal structure by adjusting the number of cubes and the stoichiometry. The MAPI perovskite structure features a (*quasi*-) orthorhombic unit cell with lattice parameters *a*, *b* and *c* equal to 8.844 Å, 8.563 Å and 12.592 Å, respectively (see Fig. S1a in the SI).[96] In addition, the MAPI perovskite structure can be also described as a (*quasi*-)cubic unit cell with *a*, *b* and *c* values of 12.467 Å, 12.467 Å and 13.123 Å, respectively

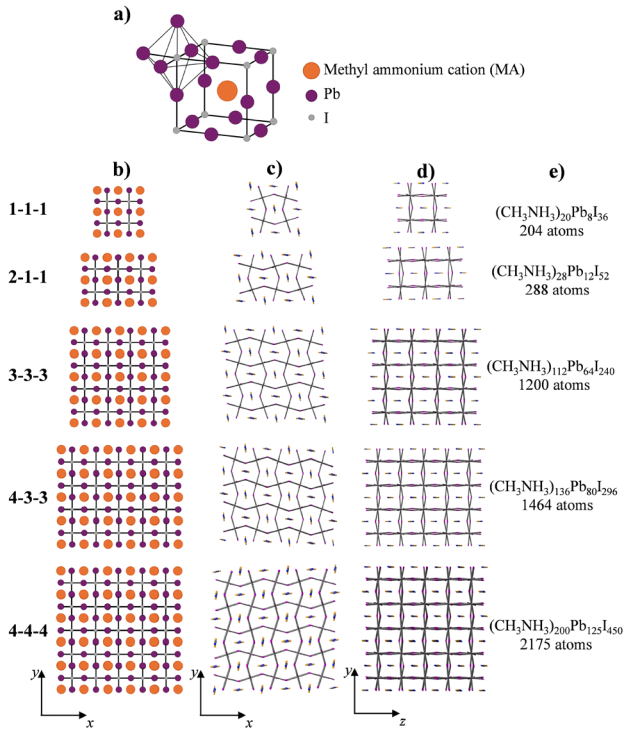

Fig. 1 (a) Definition of the perovskite crystal unit-cell. (b) Schematic representation of cluster models using circles and lines along the x–y axis. Orange, purple and grey colors represent methylammonium, Pb and I ions, respectively; (c) and (d) constructed cluster models from the experimental unit-cell along the x–y and y–z axes, respectively. C, N, Pb and I atoms are shown in blue, orange, ray and purple, respectively. Hydrogen atoms are omitted for clarity. (e) Stoichiometry and total number of atoms.

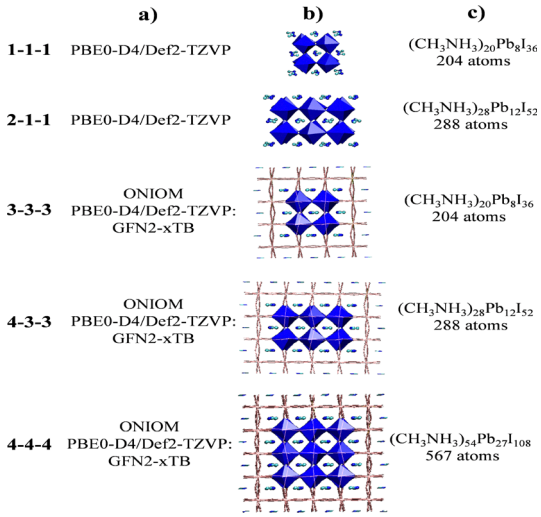

Fig. 2 Methodology applied for the study of electronic properties (absorption properties were computed using TD-DFT). (a) Selected theoretical level; (b) representation using an octahedral model of the regions studied at the PBE0-D4/Def2-TZVP level. For clusters **1-1-1** and **2-1-1**, the entire system was treated at this level. For the systems treated within the ONIOM approach, the region of interest is represented through an octahedra model, while the rest of the system is represented using a wireframe. Hydrogens atoms are omitted for clarity; (c) stoichiometry and number of atoms. For clusters **1-1-1** and **2-1-1**, the values refer to the whole cluster. For clusters **3-3-3**, **4-3-3** and **4-4-4**, the values refer to the atoms included in the high-level region.

(see Fig. S1b). For convenience, in this work, we have used this cubic unit cell, which simplifies the replication process along the axes, allowing for a better match with the number of cubes along each axis, thus facilitating the construction of the cluster.

Fig. 2 provides a summary of the methodology employed to study the electronic structure using the PBE0 functional. As previously mentioned, only clusters **1-1-1** and **2-1-1** were studied at the PBE0-D4/Def2-TZVP theoretical level. This theoretical level

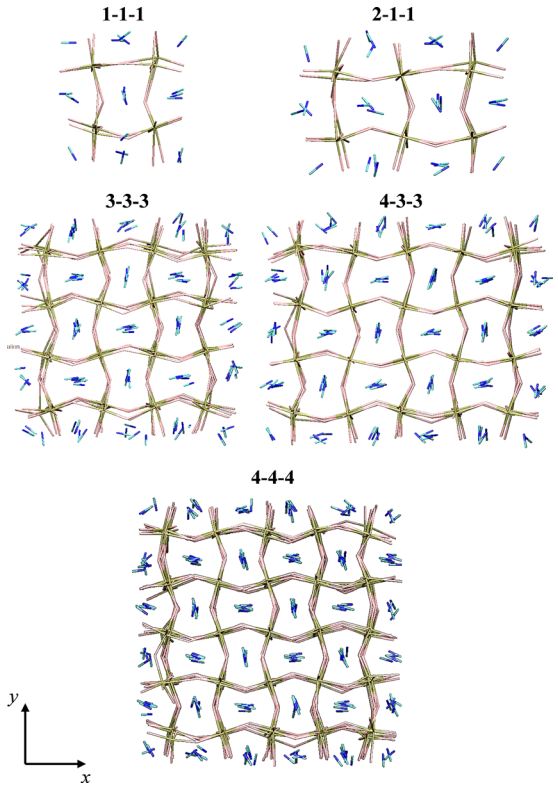

Fig. 3 Optimized structures for cluster models **1-1-1**, **2-1-1**, **3-3-3**, **4-3-3** and **4-4-4** with GFN2-xTB method. Hydrogen atoms are omitted for clarity.

Table 1 Main structural parameters for optimized cluster models with GFN2-xTB

	$d_{\text{Pb-I,average}}$[bcdf] (Å)	RMSD (Å)	Unit cell parameters[ef] a (Å)	b (Å)	c (Å)
1-1-1	3.28 (0.21%)	1.00	—	—	—
2-1-1	3.22 (2.04%)	0.96	—	—	—
3-3-3	3.18 (3.26%)	0.56	12.41 (0.43%)	12.21 (2.07%)	12.81 (2.42%)
4-3-3	3.21 (2.34%)	0.37	12.25 (1.77%)	12.40 (0.59%)	12.83 (2.24%)
4-4-4	3.20 (2.65%)	0.29	12.14 (2.63%)	12.42 (0.40%)	12.67 (3.52%)
Exp.[a]	3.29		12.47	12.47	13.12

[a] Experimental data taken from Varadwaj *et al.*[96] [b] $d_{\text{Pb-I,average}}$ refers to the average values of all Pb-I distances. See Tables SI–SV for more details. [c] The experimental unit-cell exhibits three Pb-I distances: 3.343 Å, 3.258 Å and 3.259 Å. The table collects their average value. [d] For clusters **3-3-3**, **4-3-3** and **4-4-4**, only the Pb-I distances within the central regions were considered. [e] Unit cell parameters were only measured for the central region of clusters **3-3-3**, **4-3-3** and **4-4-4**. [f] Values in parenthesis stand for the relative error with respect to the experimental value.

should be computationally prohibitive for the remaining systems. For large clusters (**3-3-3**, **4-3-3** and **4-4-4**), a two-layer ONIOM approach was applied. In ONIOM calculations, the inner region of the cluster was selected as the region of interest to be treated at the high-level (PBE0-D4/Def2-TZVP). The selection of atoms included in the high-level was performed following the two criteria described above: preserving the chemical environment of the bulk phase and maintaining electroneutrality. Thus, for systems **3-3-3** and **4-3-3**, the inner region corresponds in size and stoichiometry to clusters **1-1-1** and **2-1-1**, respectively.

Main structural parameters

The optimized structures for cluster models **1-1-1**, **2-1-1**, **3-3-3**, **4-3-3** and **4-4-4** using the GFN2-xTB method are displayed in Fig. 3, while Table 1 collects main structural parameters. When examining the octahedral environment around the Pb atoms, we noticed that all cluster models are distorted, especially clusters **1-1-1** and **2-1-1**.

Structural distortions arise from the absence of some MA needed to achieve electrically neutral structures. For clusters **3-3-3**, **4-3-3** and **4-4-4** these distortions are located at the borders of the cluster, allowing the central region to remain largely unaffected.

In Table 1, the average Pb–I distance ($d_{\mathrm{Pb-I,average}}$) represents the average distances of all Pb–I distances in the cluster. Note that for larger clusters (**3-3-3**, **4-3-3** and **4-4-4**), only the inner region of the cluster has been considered, which would have size and stoichiometry comparable to those of systems **1-1-1**, **2-1-1** and 2-2-2. The average Pb–I distance takes values around 3.22 Å, which is close to the experimental value (experimental 3.29 Å). Although average Pb–I distances approach the experimental value, there is a significant variability around $d_{\mathrm{Pb-I,average}}$ (see Tables SI–SV in the SI). As the system size increases, the dispersion of Pb–I distances decreases. Table 1 also reports the Root Mean Square Deviations (RMSD) between the optimized structures and the experimental unit-cell. All clusters lead to RMSD values below 1 Å. Furthermore, RMSD values improve with the system size. Smaller systems (**1-1-1** and **2-1-1**) show RMSD values around 0.98 Å, whereas larger clusters exhibit significant improvement.

The lattice parameters *a*, *b* and *c* have been measured for the central region of the clusters **3-3-3**, **4-3-3** and **4-4-4**. The calculated values are in good agreement with experimental data. The deviation of the optimized values from experimental data

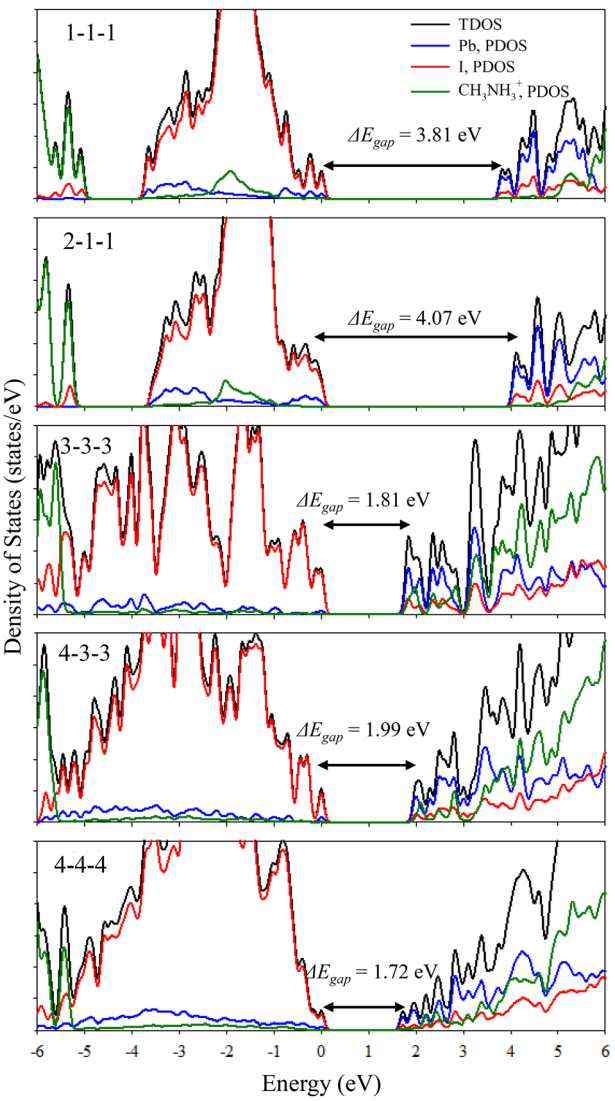

Fig. 4 Density of States for clusters **1-1-1**, **2-1-1**, **3-3-3**, **4-3-3** and **4-4-4** calculated at PBE0-D4/Def2-TZVP level. For systems **3-3-3**, **4-3-3** and **4-4-4** an ONIOM approach was applied (see Fig. 2 for more details). The energy is set with respect to the valence band maximum. The PDOS and TDOS distributions have been estimated by fitting to a Gaussian distribution with a FWHM = 0.005 atomic units.

Table 2 Molecular orbital energies for clusters **1-1-1**, **2-1-1**, **3-3-3**, **4-3-3** and **4-4-4** calculated at PBE0-D4/Def2-TZVP level. For systems **3-3-3**, **4-3-3** and **4-4-4** an ONIOM approach was applied (see Fig. 2 for more details). The zero of energy has been set at the HOMO energy. Units are in eV

	1-1-1	**2-1-1**	**3-3-3**	**4-3-3**	**4-4-4**
HOMO−9	−0.93	−0.58	−0.93	−0.89	−0.58
HOMO−8	−0.86	−0.47	−0.86	−0.82	−0.56
HOMO−7	−0.77	−0.43	−0.68	−0.76	−0.48
HOMO−6	−0.75	−0.37	−0.59	−0.68	−0.45
HOMO−5	−0.72	−0.32	−0.54	−0.68	−0.41
HOMO−4	−0.63	−0.29	−0.42	−0.47	−0.37
HOMO−3	−0.48	−0.21	−0.39	−0.43	−0.35
HOMO−2	−0.28	−0.14	−0.30	−0.32	−0.29
HOMO−1	−0.20	−0.09	−0.13	−0.28	−0.16
HOMO	0.00	0.00	0.00	0.00	0.00
LUMO	3.81	4.07	1.81	1.99	1.72
LUMO+1	3.96	4.12	1.86	2.10	1.91
LUMO+2	4.20	4.16	1.98	2.29	2.00
LUMO+3	4.24	4.26	2.09	2.46	2.19
LUMO+4	4.32	4.31	2.34	2.49	2.22
LUMO+5	4.41	4.46	2.37	2.58	2.39
LUMO+6	4.47	4.52	2.52	2.65	2.42
LUMO+7	4.50	4.54	2.58	2.76	2.50
LUMO+8	4.51	4.55	2.70	2.80	2.50
LUMO+9	4.77	4.58	2.84	2.84	2.63
$\Delta E_{\mathrm{gap}}{}^{a}$	3.81	4.07	1.81	1.99	1.72

[a] ΔE_{gap} defined as the energy difference between HOMO and LUMO orbitals.

ranges from 0.43% to 3.57%, with the largest deviations found in lattice parameter *c*.

Our results demonstrate that GFN2-xTB provides good accuracy for studying the structure of the MAPI perovskite using non-periodic calculations, with accuracy comparable to periodic DFT calculations.[23,67] It is also worth noting the lower computational cost of GFN2-xTB method, which enables the study of larger cluster models in comparison to previous works.[92,103,106,107]

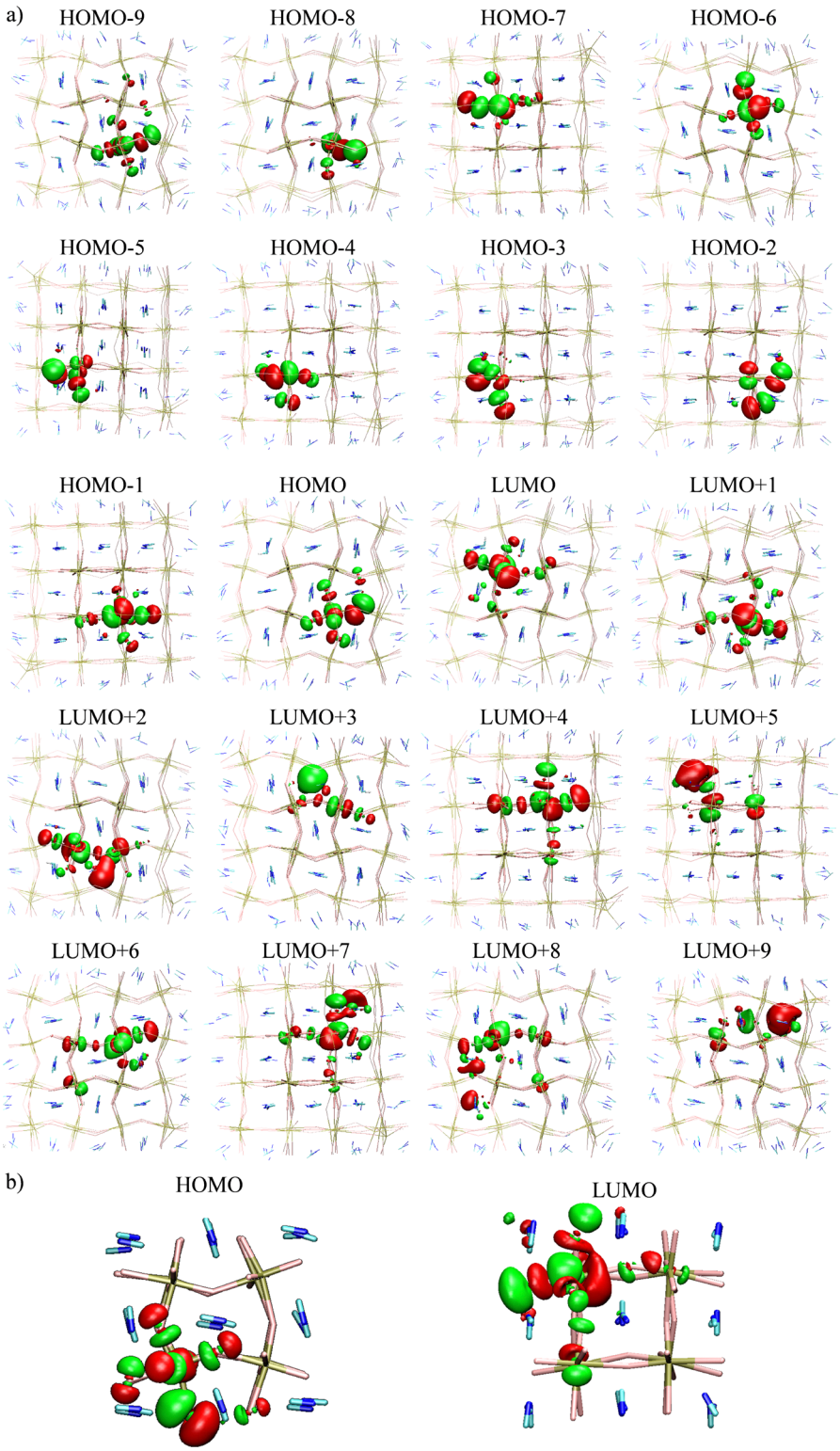

Fig. 5 (a) Frontier molecular orbital distributions for cluster **3-3-3** (isosurfaces value 0.02 atomic units). H atoms have been omitted for clarity. (b) Emphasis on the HOMO and LUMO orbitals. For clarity, atoms not included in the high-level regions have been omitted.

Optoelectronic properties

Electronic structure. The total density of states (TDOS) for the optimized cluster models, calculated at PBE0-D4/Def2-TZVP level (see Fig. 2 for more details), are shown in Fig. 4. In non-periodic calculations, the TDOS diagram is obtained from discrete energy levels of molecular orbitals. Table 2 and Table SVI present the energies of the frontier molecular orbitals. Thus, the valence band (VB) and conduction band (CB) arise from the last occupied molecular orbitals and the first unoccupied molecular orbitals, respectively. Specifically, the HOMO (highest occupied molecular orbital) of the clusters corresponds to the valence band maximum (VBM) of the bulk material, while the LUMO (lowest unoccupied molecular orbital) corresponds to the conduction band minimum (CBM). As expected for small clusters,[92,103,106,107] the bandgap (ΔE_{gap}), measured as the energy difference between the VBM and the CBM, is strongly overestimated compared to bulk material ($\sim$1.6–1.8 eV)[51] for cluster models **1-1-1** and **2-1-1** due to nanosizing effects. However, for clusters **3-3-3**, **4-3-3** and **4-4-**

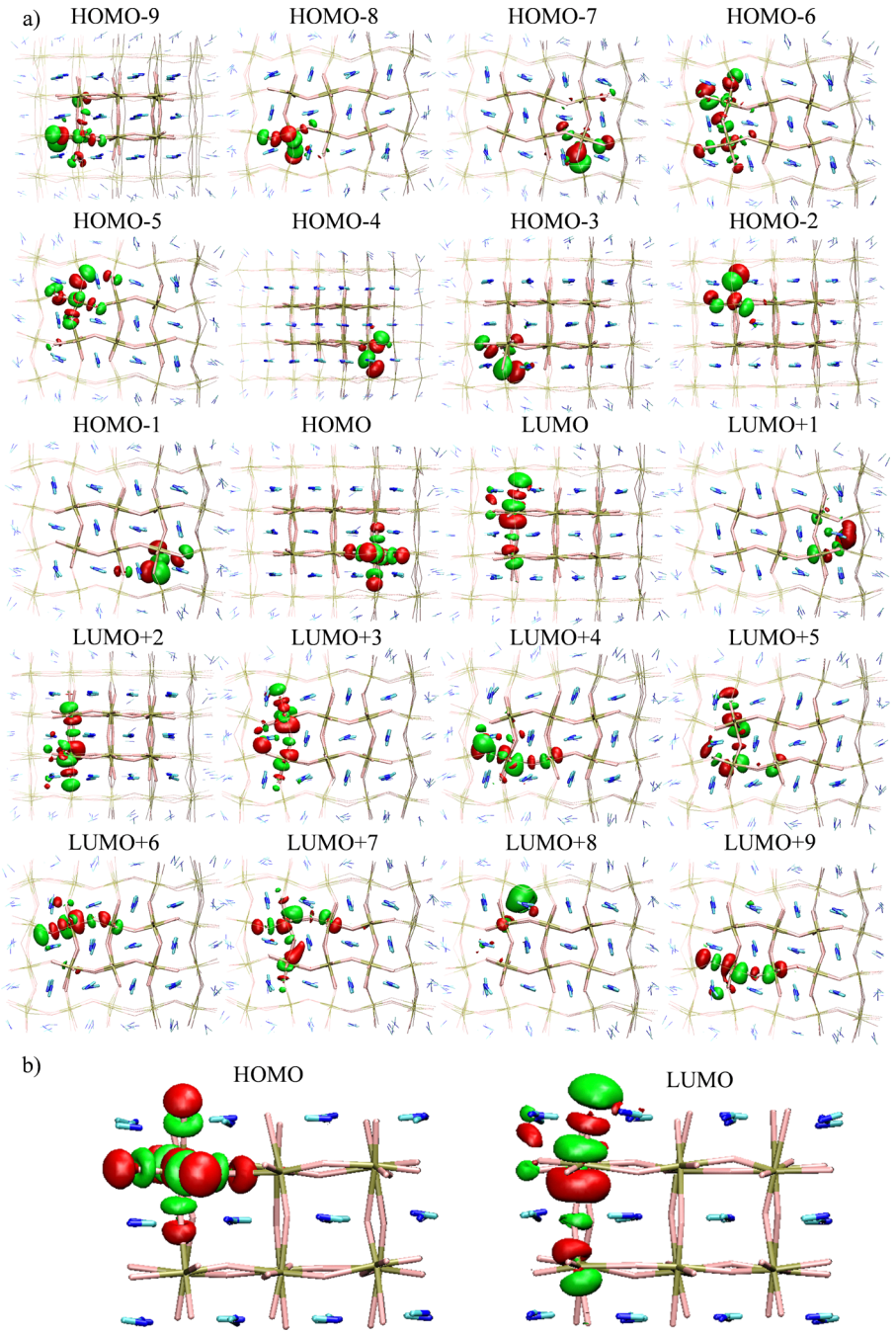

Fig. 6 (a) Frontier Molecular orbital distributions for cluster **4-3-3** (isosurfaces value 0.02 atomic units). H atoms have been omitted for clarity. (b) Emphasis on the HOMO and LUMO orbitals. For clarity, atoms not included in the high-level regions have been omitted.

4, there is a considerable improvement in the ΔE_{gap} values, which are 1.81 eV, 1.99 eV and 1.72 eV, respectively. Thus, our results for large clusters (**3-3-3**, **4-3-3** and **4-4-4**) are in good agreement with experimental value and are consistent with previously reported periodic DFT or GW + SOC results (~1.6–1.8 eV).[43,51,52,57–59,62–65,67–71]

For all systems, a detailed analysis of the Projected Density of States (PDOS) shows that the VB is mainly due to I atoms, with some contributions of Pb, while the CB is mainly contributed by Pb, with a small contribution of I. The contributions from MA cations appear further from the band edges. As an example, Fig. 5 and 6 display the spatial distributions of the frontiers orbitals for clusters **3-3-3** and **4-3-3**. Similar results are obtained for the remaining systems. In agreement with the PDOS, higher occupied molecular orbitals (which define the VB) are mainly due to I atoms and a small contribution from Pb, while the lower unoccupied molecular orbitals (defining the CB) mainly come from Pb with a small contribution from iodine. Focusing on the orbitals defining the band edges, the HOMO is mainly due to the overlap of Pb 6s-orbitals and I 5p-orbitals while the LUMO predominantly comes from Pb 6p-orbitals, with a small contribution from I 5p-orbitals. Consequently, the PDOS and molecular orbital analysis reproduce the well-established picture obtained from periodic calculations, where the VB is mainly dominated by I 5p-orbitals with some Pb 6s-contribution, while the CB is primarily derived from Pb 6p-states.[43,51,52,57–59,62–65,67–71]

Optical absorption. Optical absorption properties were calculated using TD-DFT, concretely TD-PBE0-D4/Def2-TZVP. Again, for larger systems (**3-3-3**, **4-3-3** and **4-4-4**), a two-layer ONIOM approach was applied (see Fig. 2). For each system, the first 50 excited states were required to get excitation of states above 1.0 eV above the CBM, which is computationally demanding. In fact, for system **4-4-4** only the first 10 excited states have been computed with a computational cost comparable to that of the system **4-3-3**.

Optical absorption spectra of the cluster models are shown in Fig. 7, while Table 3 collects the calculated vertical excitation energies (ΔE_{TD}), oscillator strengths (f) and nature (defined as the main contribution) of the first five excited states. See Tables SVII-SXI in the SI for more details about the first 50 excited

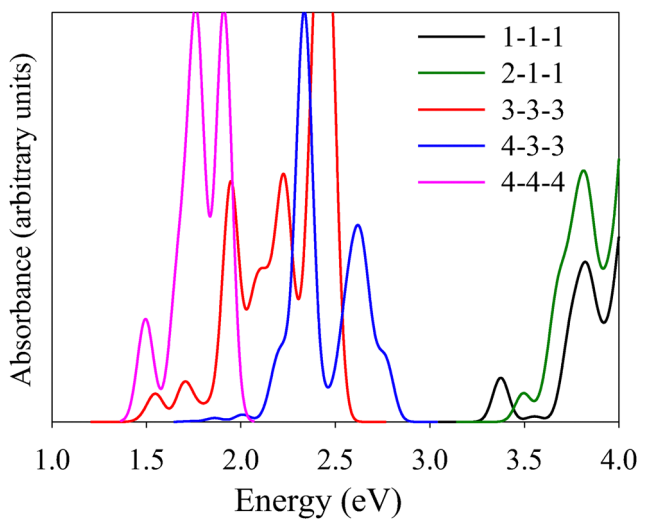

Fig. 7 Optical Absorption spectra calculated for cluster models at TD-at PBE0-D4/Def2-TZVP level. For systems **3-3-3**, **4-3-3** and **4-4-4** an ONIOM approach was applied (see Fig. 2 for more details). The spectra were obtained by fitting each transition to a Gaussian distribution with a FWHM = 0.1 eV.

Table 3 Calculated vertical excitations energies (ΔE_{TD}), oscillator strengths (f) and main configurations for clusters using TD-DFT for the first five excited states

	ΔE_{TD} (eV)	f	Configuration[a]
1-1-1			
1	3.37	0.0496	HOMO−2 → LUMO (75%)
			HOMO−1 → LUMO (9%)
			HOMO → LUMO (5%)
2	3.46	0.0004	HOMO−2 → LUMO (6%)
			HOMO → LUMO (89%)
3	3.55	0.0053	HOMO−1 → LUMO (7%)
			HOMO → LUMO+1 (87%)
4	3.58	0.0011	HOMO−2 → LUMO (6%)
			HOMO−1 → LUMO (78%)
			HOMO → LUMO+1 (8%)
5	3.72	0.0292	HOMO → LUMO+2 (45%)
			HOMO → LUMO+3 (11%)
			HOMO → LUMO+4 (25%)
			HOMO → LUMO+7 (5%)
2-1-1			
1	3.49	0.0434	HOMO−2 → LUMO (73%)
			HOMO → LUMO (6%)
2	3.61	0.0247	HOMO−2 → LUMO (5%)
			HOMO → LUMO (83%)
3	3.65	0.0512	HOMO−3 → LUMO+1 (9%)
			HOMO−1 → LUMO (11%)
			HOMO−1 → LUMO+1 (22%)
			HOMO−1 → LUMO+2 (24%)
4	3.68	0.1229	HOMO−6 → LUMO+1 (16%)
			HOMO−5 → LUMO+1 (8%)
			HOMO−3 → LUMO+1 (18%)
			HOMO−3 → LUMO+2 (9%)
			HOMO−1 → LUMO+2 (16%)
5	3.72	0.0265	HOMO−3 → LUMO+1 (6%)
			HOMO−1 → LUMO (5%)
			HOMO−1 → LUMO+1 (38%)
			HOMO−1 → LUMO+2 (7%)
			HOMO−1 → LUMO+4 (11%)
			HOMO → LUMO+1 (9%)
3-3-3			
1	1.5	0.016	HOMO → LUMO (97%)
2	1.55	0.1048	HOMO → LUMO+1 (96%)
3	1.64	0.0031	HOMO−1 → LUMO (96%)
4	1.69	0.0007	HOMO−1 → LUMO+1 (87%)
			HOMO → LUMO+2 (7%)
5	1.7	0.1504	HOMO−1 → LUMO+1 (8%)
			HOMO → LUMO+2 (88%)
4-3-3			
1	1.74	0.0028	HOMO → LUMO (99%)
2	1.86	0.0151	HOMO → LUMO+1 (98%)
3	2.01	0.0274	HOMO → LUMO+2 (98%)
4	2.03	0.0001	HOMO−1 → LUMO (98%)
5	2.06	0.0002	HOMO−2 → LUMO (98%)
4-4-4			
1	1.5	0.0017	HOMO → LUMO (99%)
2	1.65	0.0012	HOMO−1 → LUMO (99%)
3	1.69	0.0017	HOMO → LUMO+1 (99%)
4	1.76	0.0059	HOMO−2 → LUMO (98%)
5	1.78	0.0006	HOMO → LUMO+2 (99%)

[a] Percentage contribution in parentheses.

states. Qualitatively, all systems follow similar trends, where the lowest ΔE_{TD} value corresponds to a HOMO → LUMO transitions. Therefore, around the fundamental gap of MAPI, only I and Pb are the main responsible for its optical absorption features.[23] As observed in the density of states, the main difference between systems is related to the ΔE_{TD} value as a function of the system size. Again, for cluster **1-1-1** and **2-1-1** the lowest ΔE_{TD} is strongly overestimated due to nanosizing effects, leading to a considerable blue-shifting of the onset compared to experimental data.[51] However, for larger clusters (**3-3-3**, **4-3-3** and **4-4-4**), there is a considerable improvement in ΔE_{TD} (1.50 eV, 1.74 eV and 1.50 eV, respectively), in good agreement with experimental value (~1.6–1.8 eV).

TD-DFT calculations are less commonly applied in periodic systems, mainly due to their high computational cost and implementation complexity.[155,156] In periodic calculations, optical properties are commonly computed within the dipole approximation by evaluating the imaginary part of the dielectric function using the random phase approximation (RPA).[157,158] More accurate results can be achieved by combining GW with the Bethe–Salpeter equation (BSE),[159,160] which explicitly accounts for electron–hole interactions. Our TD-DFT results for large clusters (**3-3-3**, **4-3-3** and **4-4-4**) are in good agreement with experimental data and computed optical properties previously reported using periodic DFT or GW + SOC methods.[43,51,52,57–59,62–65,67–71] It should be also noted that the proposed non-periodic framework for large systems enables the use of hybrid functional such as PBE0 for systems with more than 1000 atoms through the ONIOM + EE scheme. The computational cost of the ONIOM approach is comparable to that of much smaller cluster models, since the high-level calculation is restricted to a reduced region of interest. This represents an advantage over periodic calculation with DFT or GW + SOC approaches, whose computational cost scales steeply with system size. From a computational cost perspective, system **3-3-3** and **4-3-3** have a similar cost to systems **1-1-1** and **2-1-1**, respectively. The ONIOM approach involves three calculations: two single-points with GFN2-xTB method (one on the region of interest and another on the whole system) and (TD-)DFT on the high-level region (similar to that for the system **1-1-1**). For example, in system **3-3-3**, GFN2-xTB calculations account for less than 4% of the total computational time. Further, the two-layer ONIOM approach applied here accurately calculates the electronic structure and optical absorption of the MAPI perovskite using non-periodic calculations, highlighting the importance of including electrostatic polarization effects.

Conclusions

We present a robust computational framework to study the structural and optoelectronic properties of metal halide perovskites, strategically combining xTB, DFT and ONIOM methods. This framework effectively harnesses the strengths of each method to provide accurate results while maintaining computational efficiency.

As a reference compound, we focused on the widely studied MAPI perovskite. Firstly, based on the unit-cell structure, several cluster models (ranging from 204 to 2175 atoms) were constructed to preserve the chemical environment of the constituent ions and maintain electroneutrality. These cluster models were optimized using GFN2-xTB method. Our results demonstrate that GFN2-XTB provides accurate structural parameters comparable to those obtained from DFT calculations and experimental data. The accuracy of the optimized structures considerably improves for larger clusters (>100 atoms), systems whose study would be computationally prohibitive using DFT methods.

Optoelectronic properties (electronic structure and optical absorption) were computed using DFT (TD-DFT for optical absorption) at PBE0-D4/Def2-TZVP level. As expected, for smaller clusters (up to ~200 atoms), our results qualitatively capture the main features of valence and conduction bands, although there is a considerable bandgap overestimation due to nanosizing effects.

For large clusters (>1000 atoms), we applied a two-layer ONIOM scheme which treats the region of interest (the inner region of the cluster) with PBE0-D4/Def2-TZVP, while the surrounding environment is treated with GFN2-xTB along with electrostatic embedding. This approach accurately describes the main characteristics of the electronic structure as well as the optical absorption features, highlighting the key role of reproducing the electrostatic environment. Our results demonstrate that the proposed cluster-based ONIOM + EE framework yields electronic structure features (such as bandgap and band-edges composition) in good agreement with experimental and previously reported periodic results with a reduced computational cost. Additionally, the ONIOM setup is considerably streamlined by requiring only the selection of the atoms included in the high-level region following both above-mentioned criteria (*i.e.*, preserving the chemical environment and maintaining electroneutrality), without causing a significant increase in computational costs compared to smaller clusters.

Author contributions

Adrián Moro-Marín: writing – original draft, investigation. Gregorio García: writing – review & editing, writing – original draft, visualization, resources, methodology, investigation, formal analysis, data curation, conceptualization. Silverio Coco: writing – review & editing. All authors have read and agreed to the published version of the manuscript.

Conflicts of interest

There are no conflicts to declare.

Data availability

The data supporting the conclusions are provide in the manuscript and supplementary information (SI). Supplementary

information is available. See DOI: https://doi.org/10.1039/d6cp00073h.

Acknowledgements

This research has made use of the high performance computing resources of the Castilla y León Supercomputing Center (SCAYLE, https://www.scayle.es), financed by the European Regional Development Fund (ERDF).

References

1 C. Yang, W. Hu, J. Liu, C. Han, Q. Gao, A. Mei, Y. Zhou, F. Guo and H. Han, *Light: Sci. Appl.*, 2024, **13**, 227.
2 G. Dastgeer, S. Nisar, M. W. Zulfiqar, J. Eom, M. Imran and K. Akbar, *Nano Energy*, 2024, **132**, 110401.
3 T. D. Raju, V. Murugadoss, K. A. Nirmal, T. D. Dongale, A. V. Kesavan and T. G. Kim, *Adv. Powder Mater.*, 2025, **4**, 100275.
4 J. Y. Kim, J.-W. Lee, H. S. Jung, H. Shin and N.-G. Park, *Chem. Rev.*, 2020, **120**, 7867–7918.
5 A. K. Jena, A. Kulkarni and T. Miyasaka, *Chem. Rev.*, 2019, **119**, 3036–3103.
6 P. Roy, N. Kumar Sinha, S. Tiwari and A. Khare, *Sol. Energy*, 2020, **198**, 665–688.
7 H. J. Snaith, *J. Phys. Chem. Lett.*, 2013, **4**, 3623–3630.
8 S. Khatoon, S. Kumar-Yadav, V. Chakravorty, J. Singh, R. Bahadur-Singh, M. S. Hasnain and S. M. M. Hasnain, *Mater. Sci. Energy Technol.*, 2023, **6**, 437–459.
9 S. D. Stranks and H. J. Snaith, *Nat. Nanotech.*, 2015, **10**, 391–402.
10 P. Gao, M. Grätzel and M. K. Nazeeruddin, *Energy Environ. Sci.*, 2014, **7**, 2448–2463.
11 M. Grätzel, *Acc. Chem. Res.*, 2017, **50**, 487–491.
12 J. Han, K. Park, S. Tan, Y. Vaynzof, J. Xue, E. W.-G. Diau, M. G. Bawendi, J.-W. Lee and I. Jeon, *Nat. rev. Methods Primers*, 2025, **5**, 3.
13 H. S. Jung and N. G. Park, *Small*, 2015, **11**, 10–25.
14 N. G. Park, *Acc. Chem. Res.*, 2026, **59**, 40–51.
15 G. Nazir, S.-Y. Lee, J.-H. Lee, A. Rehman, J.-K. Lee, S. I. Seok and S.-J. Park, *Adv. Mater.*, 2022, **34**, 2204380.
16 C. C. Stoumpos and M. G. Kanatzidis, *Adv. Mater.*, 2016, **28**, 5778–5793.
17 C. C. Stoumpos and M. G. Kanatzidis, *Acc. Chem. Res.*, 2015, **48**, 2791–2802.
18 I. W. Gilley, T. E. Wiggins, E. H. Sargent and M. G. Kanatzidis, *Acc. Chem. Res.*, 2025, **58**, 2243–2254.
19 L. A. Castriotta, *ACS Energy Lett.*, 2026, **11**, 2378–2381.
20 Best Research-Cell Efficiency Chart, NREL. https://www.nlr.gov/pv/cell-efficiency.
21 N. Li, X. Niu, Z. Dong, J. Hu, R. Luo, S. Yang, Q. Zhou, Z. Shi, J. Chen, X. Du, L. K. Lee, Y. Wang, X. Guo, X. Wang, C.-W. Qiu, M. Lin, R. He, X. Zhang, Y. Chen, M. Wu and Y. Hou, *Science*, 2025, **390**, eadz3698.
22 T. Wang, B. Daiber, J. M. Frost, S. A. Mann, E. C. Garnett, A. Walsh and B. Ehrler, *Science*, 2017, **10**, 509–515.
23 E. Menéndez-Proupin, P. Palacios, P. Wahnón and J. C. Conesa, *Phys. Rev. B: Condens. Matter Mater. Phys.*, 2014, **90**, 045207.
24 A. Filippetti, A. Mattoni, C. Caddeo, M. I. Saba and P. Delugas, *Phys. Chem. Chem. Phys.*, 2016, **18**, 15352–15362.
25 G. Xing, N. Mathews, S. Sun, S. S. Lim, Y. M. Lam, M. Grätzel, S. Mhaisalkar and T. C. Sum, *Science*, 2013, **342**, 344.
26 A. L. Montero-Alejo, E. Menéndez-Proupin, P. Palacios, P. Wahnón and J. C. Conesa, *J. Phys. Chem. C*, 2017, **121**, 26698–26705.
27 Y. Wang, W.-H. Fang, R. Long and O. V. Prezhdo, *J. Phys. Chem. Lett.*, 2019, **10**, 1617–1623.
28 M. B. Johnston and L. M. Herz, *Acc. Chem. Res.*, 2016, **49**, 146–154.
29 E. Menéndez-Proupin, C. L. Beltrán Ríos and P. Wahnón, *Phys. Status Solidi RRL*, 2015, **9**, 559–563.
30 N.-G. Park, *Mater. Today*, 2015, **18**, 65–72.
31 B. Conings, J. Drijkoningen, N. Gauquelin, A. Babayigit, J. D'Haen, L. D'Olieslaeger, A. Ethirajan, J. Verbeeck, J. Manca, E. Mosconi, F. De Angelis and H. G. Boyen, *Adv. Energy Mater.*, 2015, **5**, 1500477.
32 A. Babayigit, A. Ethirajan, M. Muller and B. Conings, *Nat. Mater.*, 2016, **15**, 247–251.
33 P. Sánchez-Palencia, G. García, P. Wahnón and P. Palacios, *Inorg. Chem. Front.*, 2021, **8**, 3803–3814.
34 P. Sánchez-Palencia, G. García, P. Wahnón and P. Palacios, *Inorg. Chem. Front.*, 2022, **9**, 1337–1353.
35 G. E. Eperon, G. M. Paterno, R. J. Sutton, A. Zampetti, A. A. Haghighirad, F. Cacialli and H. J. Snaith, *J. Mater. Chem. A*, 2015, **3**, 19688–19695.
36 C. Shen, T. Ye, P. Yang and G. Chen, *Adv. Mater.*, 2024, **36**, e2401498.
37 X. Liu, J. Li, X. Cui, X. Wang and D. Yang, *J. Mater. Chem. C*, 2023, **11**, 426–455.
38 X. Liu, J. Li, X. Cui, X. Wang and D. Yang, *J. Mater. Chem. C*, 2023, **11**, 426–455.
39 G. Giorgi, J.-I. Fujisawa, H. Segawa and K. Yamashita, *J. Phys. Chem. Lett.*, 2013, **4**, 4213–4216.
40 G. Giorgi, J.-I. Fujisawa, H. Segawa and K. Yamashita, *J. Phys. Chem. C*, 2014, **118**, 12176–12183.
41 G. Giorgi, J.-I. Fujisawa, H. Segawa and K. Yamashita, *J. Phys. Chem. C*, 2015, **119**, 4694–4701.
42 A. Amat, E. Mosconi, E. Ronca, C. Quarti, P. Umari, M. K. Nazeeruddin, M. Grätzel and F. De Angelis, *Nano Lett.*, 2014, **14**, 3608–3616.
43 J. Even, L. Pedesseau, J.-M. Jancu and C. Katan, *J. Phys. Chem. Lett.*, 2013, **4**, 2999–3005.
44 T. Baikie, Y. Fang, J. M. Kadro, M. Schreyer, F. Wei, S. G. Mhaisalkar, M. Graetzel and T. J. White, *J. Mater. Chem. A*, 2013, **1**, 5628–5641.
45 J. Haruyama, K. Sodeyama, L. Han and Y. Tateyama, *J. Phys. Chem. Lett.*, 2014, **5**, 2903–2909.
46 Y. Wang, T. Gould, J. F. Dobson, H. Zhang, H. Yang, X. Yao and H. Zhao, *Phys. Chem. Chem. Phys.*, 2014, **16**, 1424–1429.

47 D. A. Egger and L. Kronik, *J. Phys. Chem. Lett.*, 2014, **5**, 2728–2733.
48 G. Giorgi and K. Yamashita, *J. Mater. Chem. A*, 2015, **3**, 8981–8991.
49 E. Mosconi, A. Amat, M. K. Nazeeruddin, M. Grätzel and F. De Angelis, *J. Phys. Chem. C*, 2013, **117**, 13902–13913.
50 W.-J. Yin, T. Shi and Y. Yan, *Appl. Phys. Lett.*, 2014, **104**, 063903.
51 T. Das, G. Di Liberto and G. Pacchioni, *J. Phys. Chem. C*, 2022, **126**, 2184–2198.
52 R. A. Jishi, O. B. Ta and A. A. Sharif, *J. Phys. Chem. C*, 2014, **118**, 28344–28349.
53 A. Filippetti and A. Mattoni, *Phys. Rev. B: Condens. Matter Mater. Phys.*, 2014, **89**, 125203.
54 B. Zhang, G. Lei, S. You, W. Zhao and H. Liu, *Inorg. Chem.*, 2024, **63**, 3303–3316.
55 S. Pachori, R. Agrawal, A. Shukla and A. S. Verma, *Mater. Chem. Phys.*, 2022, **287**, 126149.
56 A. Filippetti, S. Kahmann, C. Caddeo, A. Mattoni, M. Saba, A. Bosin and M. A. Loi, *J. Mater. Chem. A*, 2021, **9**, 11812–11826.
57 L. D. Whalley, J. M. Frost, Y.-K. Jung and A. Walsh, *J. Chem. Phys.*, 2017, **146**, 220901.
58 W. Li, N. M. Atikah Zulkafli, M. H. Mamat and M. K. Yaakob, *Phys. B*, 2025, **704**, 417075.
59 D. Meggiolaro and F. De Angelis, *ACS Energy Lett.*, 2018, **3**, 2206–2222.
60 E. Mosconi, E. Ronca and F. De Angelis, *J. Chem. Phys. Lett.*, 2014, **5**, 2619–2625.
61 C. Quarti, E. Mosconi and F. De Angelis, *Phys. Chem. Chem. Phys.*, 2015, **17**, 9394–9409.
62 P. Umari, E. Mosconi and F. De Angelis, *Sci. Rep.*, 2014, **4**, 4467.
63 F. Brivio, K. T. Butler, A. Walsh and M. van Schilfgaarde, *Phys. Rev. B: Condens. Matter Mater. Phys.*, 2014, **89**, 155204.
64 M. R. Filipand and F. Giustino, *Phys. Rev. B: Condens. Matter Mater. Phys.*, 2014, **90**, 245145.
65 Y.-T. Huang, S. R. Kavanagh, D. O. Scanlon, A. Walsh and R. L. Z. Hoye, *Nanotechnology*, 2021, **32**, 132004.
66 W. Geng, C.-J. Tong, Y. Zhang and L.-M. Liu, *Adv. Theory Simul.*, 2020, **3**, 2000022.
67 G. García, P. Palacios, E. Menéndez-Proupin, A. L. Montero-Alejo, J. C. Conesa and P. Wahnón, *Sci. Rep.*, 2018, **8**, 2511.
68 R. F. Berger and J. B. Neaton, *Phys. Rev. B: Condens. Matter Mater. Phys.*, 2012, **86**, 165211.
69 M. Palummo, E. Berrios, D. Varsano and G. Giorgi, *ACS Energy Lett.*, 2020, **5**, 457–463.
70 G. Giorgi, K. Yamashita and M. Palummo, *J. Chem. Phys. Lett.*, 2018, **9**, 5891–5896.
71 M. R. Filip, G. E. Eperon, H. J. Snaith and F. Giustino, *Nat. Commun.*, 2014, **5**, 5757.
72 I. B. Garba, L. Trombini, C. Katan, J. Even, M. Zacharias, M. Kepenekian and G. Volonakis, *ACS Mater. Lett.*, 2025, **7**, 1922–1929.
73 S. M. Butorin, *ACS Appl. Energy Mater.*, 2024, **7**, 7285–7290.
74 B. Traoré, G. Bouder, W. Lafargue-Dit-Hauret, X. Rocquefelte, C. Katan, F. Tran and M. Kepenekian, *Phys. Rev. B*, 2019, **99**, 035139.
75 S. X. Tao, X. Cao and P. A. Bobbert, *Sci. Rep.*, 2017, **7**, 14386.
76 M. Ezzeldien, S. Al-Qaisi, Z. A. Alrowaili, M. Alzaid, E. Maskar, A. Es-Smairi, T. V. Vu and D. P. Rai, *Sci. Rep.*, 2021, **11**, 20622.
77 M. Moaddeli, M. Kanani and A. Grünebohm, *Phys. Chem. Chem. Phys.*, 2023, **25**, 25511–25525.
78 D. Guedes-Sobrinho, I. Guilhon, M. K. Marques and L. Teles, *J. Chem. Phys. Lett.*, 2019, **10**, 4245–4251.
79 A. S. P. Gomes, C. R. Jacob and L. Visscher, *Phys. Chem. Chem. Phys.*, 2008, **10**, 5353–5362.
80 A. M. Pessoa, J. L. C. Fajín, J. R. B. Gomes and M. N. D. S. Cordeiro, *J. Mol. Struct. THEOCHEM*, 2010, **946**, 43–50.
81 B. X. Shi, A. S. Rosen, T. Schäfer, A. Grüneis, V. Kapil, A. Zen and A. Michaelides, *Nat. Chem.*, 2025, **17**, 1688–1695.
82 Y. Li, L. Zhang, X. Sun, M. Xu, B. Liu, X. Zhao, G. Hao, J. Bai and X. Lin, *Mat. Adv.*, 2024, **5**, 5838–5844.
83 Z. Gao, G. Yan, M. Zhao, S. Xu, L. Li, H. Huang, W. Yang and X. Ding, *Sol. Energy Mater. Sol. Cells*, 2019, **202**, 110126.
84 N. Xu, X. Qi, Z. Shen, L. Hu, J. Lv, Y. Zhong, B. Wang and Z. Zou, *Nat. Rev. Phys.*, 2025, **7**, 554–564.
85 K. Miyata, D. Meggiolaro, M. T. Trinh, P. P. Joshi, E. Mosconi, S. C. Jones, F. De Angelis and X. Y. Zhu, *Sci. Adv.*, 2017, **3**, e1701217.
86 Y. Yamada and Y. Kanemitsu, *NPG Asia Mater.*, 2022, **14**, 48.
87 C. Motta and S. Sanvito, *J. Phys. Chem. C*, 2018, **122**, 1361–1366.
88 A. J. Neukirch, W. Nie, J.-C. Blancon, K. Appavoo, H. Tsai, M. Y. Sfeir, C. Katan, L. Pedesseau, J. Even, J. J. Crochet, G. Gupta, A. D. Mohite and S. Tretiak, *Nano Lett.*, 2016, **16**, 3809.
89 L. Zhou, A. J. Neukirch, D. J. Vogel, D. S. Kilin, L. Pedesseau, M. A. Carignano, A. D. Mohite, J. Even, C. Katan and S. Tretiak, *ACS Energy Lett.*, 2018, **3**, 787.
90 A. J. Neukirch, I. I. Abate, L. Zhou, W. Nie, H. Tsai, L. Pedesseau, J. Even, J. J. Crochet, A. D. Mohite, C. Katan and S. Tretiak, *J. Chem. Phys. Lett.*, 2018, **9**, 7130–7136.
91 G. Pacchioni, P. S. Bagus and F. Parmigiani. *Cluster Models for Surface and Bulk Phenomena*, Springer, US, 2013.
92 G. Giorgi, T. Yoshihara and K. Yamashita, *Phys. Chem. Chem. Phys.*, 2016, **18**, 27124.
93 H. Fang and P. Jena, *J. Phys. Chem. Lett.*, 2016, **7**, 1596–1603.
94 H. Fang and P. Jena, *J. Phys. Chem. Lett.*, 2017, **8**, 3726–3733.
95 Z. Gao, S. Chen, Y. Bai, M. Wang, X. Liu, W. Yang, W. Li, X. Ding and J. Yao, *Phys. Chem. Chem. Phys.*, 2021, **23**, 11548–11556.
96 P. R. Varadwaj, A. Varadwaj, H. M. Marques and K. Yamashita, *Sci. Rep.*, 2019, **9**, 50.
97 A. Varadwaj, P. Varadwaj and K. Yamashita, *ChemistrySelect*, 2018, **3**, 7269–7282.

98 G. Giorgi and K. Yamashita, *J. Phys. Chem. Lett.*, 2016, **7**, 888–899.
99 A. Varadwaj, P. Varadwaj and K. Yamashita, *J. Comput. Chem.*, 2017, **38**, 2802.
100 J.-I. Fujisawa and G. Giorgi, *Phys. Chem. Chem. Phys.*, 2014, **16**, 17955–17959.
101 Y. Fu, S. Poddar, B. Ren, Y. Xie, Q. Zhang, D. Zhang, B. Cao, Y. Tang, Y. Ding, X. Qiu, L. Shu, J.-F. Liao, D.-B. Kuang and Z. Fan, *ACS Nano*, 2022, **16**, 8388–8398.
102 C. M. Perez, D. Ghosh, O. Prezhdo, S. Tretiak and A. J. Neukirch, *J. Chem. Phys. Lett.*, 2021, **12**, 1005–1011.
103 A. Koliogiorgos, C. S. Garoufalis, I. Galanakis and S. Baskoutas, *ACS Omega*, 2018, **3**, 18917–18924.
104 S. L. Choon, H. N. Lim, I. Ibrahim, Z. Zainal, K. B. Tan, C. Y. Foo and C. H. Ng, *Renewable Sustainable Energy Rev.*, 2023, **171**, 113037.
105 X. Peng, Z. Lai, H. Shao, Y. Shen, Y. Meng and J. C. Ho, *npj Nanophotonics*, 2025, **2**, 42.
106 S. Manzhos, A. Pal, Y. Chen and G. Giorgi, *Phys. Chem. Chem. Phys.*, 2019, **21**, 8161–8169.
107 Y. Chen, X. Ding, L. Yang, Y. Wang, J. I. Gurti, M. Wang, W. Li, X. Wang and W. Yang, *Phys. Chem. Chem. Phys.*, 2022, **24**, 14375–14389.
108 C. S. Garoufalis, I. Galanakis, Z. Zeng, D. B. Hayrapetyan and S. Baskoutas, *Electron. Mater.*, 2021, **2**, 382.
109 J. Leveillee, C. Katan, J. Even, D. Ghosh, W. Nie, A. D. Mohite, S. Tretiak, A. Schleife and A. J. Neukirch, *Nano Lett.*, 2019, **19**, 8732–8740.
110 C. Bannwarth, E. Caldeweyher, S. Ehlert, A. Hansen, P. Pracht, J. Seibert, S. Spicher and S. Grimme, *Wiley Interdiscip. Rev.: Comput. Mol. Sci.*, 2021, **11**, e1493.
111 C. Bannwarth, S. Ehlert and S. Grimme, *J. Chem. Theory Comput.*, 2019, **15**, 1652–1671.
112 J. M. Vicent-Luna, S. Apergi and S. Tao, *J. Chem. Inf. Model.*, 2021, **61**, 4415–4424.
113 S. Raaijmakers, M. Pols, J. M. Vicent-Luna and S. Tao, *J. Phys. Chem. C*, 2022, **126**, 9587–9596.
114 C. Adamo and V. Barone, *J. Chem. Phys.*, 1999, **110**, 6158–6170.
115 E. Caldeweyher, S. Ehlert, A. Hansen, H. Neugebauer, S. Spicher, C. Bannwarth and S. Grimme, *J. Chem. Phys.*, 2019, **150**, 154122.
116 F. Weigend and R. Ahlrichs, *Phys. Chem. Chem. Phys.*, 2005, **7**, 3297–3305.
117 F. Weigend, *Phys. Chem. Chem. Phys.*, 2006, **8**, 1057–1065.
118 B. Metz, H. Stoll and M. Dolg, *J. Chem. Phys.*, 2000, **113**, 2563–2569.
119 M. Dolg and X. Cao, *Chem. Rev.*, 2012, **112**, 403–480.
120 L. W. Chung, W. M. C. Sameera, R. Ramozzi, A. J. Page, M. Hatanaka, G. P. Petrova, T. V. Harris, X. Li, Z. Ke, F. Liu, H. B. Li and K. Morokuma, *Chem. Rev.*, 2015, **115**, 5678–5796.
121 H. P. Hratchian, P. V. Parandekar, K. Raghavachari, M. J. Frisch and T. Vreven, *J. Chem. Phys.*, 2008, **128**, 034107.
122 P. Colinet, F. Neese and B. Helmich-Paris, *J. Comput. Chem.*, 2025, **46**, e27532.
123 C. Plett, A. Katbashev, S. Ehlert and S. Grimme, *Phys. Chem. Chem. Phys.*, 2023, **25**, 17860–17868.
124 M. Bursch, H. Neugebauer and S. Grimme, *Angew. Chem., Int. Ed.*, 2019, **58**, 11078–11087.
125 M. Bursch, A. Hansen and S. Grimme, *Inorg. Chem.*, 2017, **56**, 12485–12491.
126 R. Erdogan and I. Onal, *Int. J. Quantum Chem.*, 2011, **111**, 2149–2159.
127 G. F. Velardez, H. T. Lemke, D. W. Breiby, M. M. Nielsen, K. B. Møller and N. E. Henriksen, *J. Phys. Chem. A*, 2008, **112**, 8179–8187.
128 S.-Y. Yang, L. Zhao, Y.-A. Duan, Y. Geng and Z.-M. Su, *Theor. Chem. Acc.*, 2013, **132**, 1377.
129 F. Labat, I. Ciofini, H. P. Hratchian, M. J. Frisch, K. Raghavachari and C. Adamo, *J. Phys. Chem. C*, 2011, **115**, 4297–4306.
130 D. Presti, F. Labat, A. Pedone, M. J. Frisch, H. P. Hratchian, I. Ciofini, M. C. Menziani and C. Adamo, *J. Chem. Theory Comput.*, 2014, **10**, 5577–5585.
131 C. Diguet, A. Navarro, M. P. Fernández-Liencres, S. B. Jiménez-Pulido, N. A. Illán-Cabeza, J. Massue, S. Gauthier, F. Robin-le Guen, S. Achelle and J. Rodríguez-López, *Dyes Pigm.*, 2025, **236**, 112660.
132 J. Álvarez-Conde, M. P. Fernández-Liencres, S. B. Jiménez-Pulido, C. Martín, A. Navarro, J. Cabanillas-González and E. M. García-Frutos, *Adv. Funct. Mater.*, 2025, **35**, 2402859.
133 Y. Ma, M. Lv, F. Shang, C. Zhang, J. Liu and P. Zhou, *J. Phys. Chem. A*, 2022, **126**, 1666–1673.
134 M. Rivera, M. Dommett and R. Crespo-Otero, *J. Chem. Theory Comput.*, 2019, **15**, 2504–2516.
135 J. Hoja, A. List and A. D. Boese, *J. Chem. Theory Comput.*, 2024, **20**, 357–367.
136 P. S. Bagus, M. J. Sassi and K. M. Rosso, *J. Chem. Phys.*, 2019, **151**, 044107.
137 J. Su, D. Luise, I. Ciofini and F. Labat, *J. Phys. Chem. C*, 2023, **127**, 5968–5981.
138 A. Dittmer, R. Izsák, F. Neese and D. Maganas, *Inorg. Chem.*, 2019, **58**, 9303–9315.
139 F. Neese, *Wiley Interdiscip. Rev.: Comput. Mol. Sci.*, 2025, **15**, e70019.
140 F. Neese, *Wiley Interdiscip. Rev.: Comput. Mol. Sci.*, 2012, **2**, 73–78.
141 A. S. Christensen, T. Kubař, Q. Cui and M. Elstner, *Chem. Rev.*, 2016, **116**, 5301–5337.
142 E. E. Greciano, J. Calbo, J. Buendía, J. Cerdá, J. Aragó, E. Ortí and L. Sánchez, *J. Am. Chem. Soc.*, 2019, **141**, 7463–7472.
143 M. A. Martínez, A. Doncel-Giménez, J. Cerdá, J. Calbo, R. Rodríguez, J. Aragó, J. Crassous, E. Ortí and L. Sánchez, *J. Am. Chem. Soc.*, 2021, **143**, 13281–13291.
144 E. Castellanos, R. M. Gomila, R. Manha, G. Fernández, A. Frontera and B. Soberats, *J. Mater. Chem. C*, 2023, **11**, 10884–10892.
145 L. Rubert, M. F. Islam, A. B. Greytak, R. Prakash, M. D. Smith, R. M. Gomila, A. Frontera, L. S. Shimizu and B. Soberats, *Angew. Chem., Int. Ed.*, 2023, **62**, e202312223.
146 E. de Domingo, G. García, C. L. Folcia, J. Ortega, J. Etxebarria and S. Coco, *Cryst. Growth Des.*, 2023, **23**, 6812–6821.

147 E. de Domingo, G. García and S. Coco, *J. Mol. Liq.*, 2025, **431**, 127663.
148 C. Vona, D. Nabok and C. Draxl, *Adv. Theory Simul.*, 2021, **5**, 2100496.
149 P. García-Fernández, S. Ghosh, N. J. English and J. A. Aramburu, *Phys. Rev. B: Condens. Matter Mater. Phys.*, 2012, **86**, 144107.
150 E. Mosconi, P. Umari and F. De Angelis, *J. Mater. Chem. A*, 2015, **3**, 9208–9215.
151 A. Chantzis, A. D. Laurent, C. Adamo and D. Jacquemin, *J. Chem. Theory Comput.*, 2013, **9**, 4517–4525.
152 https://www.ks.uiuc.edu/Research/vmd/.
153 W. Humphrey, A. Dalke and K. Schulten, VMD: visual molecular dynamics, *J. Mol. Graph*, 1996, **14**(1), 33–38, DOI: 10.1016/0263-7855(96)00018-5.
154 W. Humphrey, A. Dalke and K. Schulten, *J. Mol. Graphics*, 1996, **14**, 33–38.
155 G. Onida, L. Reining and A. Rubio, *Rev. Mod. Phys.*, 2002, **74**, 601–659.
156 K. Hanasaki, Z. A. Ali, M. Choi, M. Del Ben and B. M. Wong, *J. Comput. Chem.*, 2023, **44**, 980–987.
157 M. Gajdoš, K. Hummer, G. Kresse, J. Furthmüller and F. Bechstedt, *Phys. Rev. B: Condens. Matter Mater. Phys.*, 2006, **73**, 045112.
158 G. Kresse and J. Furthmüller, *Phys. Rev. B: Condens. Matter Mater. Phys.*, 1996, **54**, 11169.
159 S. Albrecht, L. Reining, R. Del Sole and G. Onida, *Phys. Rev. Lett.*, 1998, **80**, 4510–4513.
160 M. Rohlfing and S. G. Louie, *Phys. Rev. Lett.*, 1998, **81**, 2312–2315.